sustainability

MDPI

Article

Stress Characteristics and Rock Burst Prediction of the Xuefeng Mountain No.1 Tunnel: On-Site and Numerical Investigations

Guo Xiang [1], Xiaohua Zhang [1], Shengnian Wang [1,2,*], Sanyou Wu [3], Xinming Pan [1] and Dehui Xu [1]

[1] College of Transportation Science and Engineering, Nanjing Tech University, Nanjing 211816, China; 202162126014@njtech.edu.cn (G.X.); 202362261281@njtech.edu.cn (X.Z.); 202261125014@njtech.edu.cn (X.P.); 202261225062@njtech.edu.cn (D.X.)

[2] Jiangsu Province Engineering Research Center of Transportation Infrastructure Security Technology, Nanjing 211816, China

[3] Basis International School Nanjing, Nanjing 210023, China; sanyou_nj@163.com

* Correspondence: shengnian.wang@njtech.edu.cn; Tel.: +86-137-70655160

Abstract: The risk level and disaster scale of rock bursts in deeply buried and highly stressed tunnels are commonly high, posing serious threats to their construction safety. This study employed a combination of on-site measurements and discrete-continuous coupled numerical simulations to analyze the geo-stress distribution characteristics of surrounding rock masses in the Xuefeng Mountain No.1 Tunnel. The evolution processes of rock burst failure in surrounding rock masses with different lithologies and buried at different depths were discussed. The risk of rock bursts along this long tunnel was predicted using the stress–strength ratio criterion and the energy method. The results showed that the principal stress values of surrounding rock masses in the Xuefeng Mountain No.1 Tunnel followed a distribution pattern of $\sigma_x > \sigma_y > \sigma_z$ (where x, y, and z denoted the directions of tunnel cross-section and tunnel axis and the direction perpendicular to the ground), with average stress levels exceeding 20 MPa. It should be a typical tunnel dominated by horizontal tectonic stress. Stress concentration and elastic strain energy accumulation zones in this tunnel were mainly located at the bottom, and the largest displacements always occurred at the inverted arch. The main characteristics of rock burst failure in this tunnel included the sheet-like splitting of rock mass layers and the ejection of rock blocks. The risk evaluation of rock bursts across different sections of the tunnel, considering various rock types and buried depths, presented that these deeply buried slate and granite exhibited the highest risk level when assessed using the elastic strain energy index criterion. The comparative analysis between the elastic strain energy method and the stress–strength ratio criterion showed that the evaluation results obtained by the latter were more conservative. The findings of this study can provide a valuable reference for cognizing the geo-stress characteristics and predicting rock bursts in the surrounding rock masses of deep-buried and highly stressed tunnels.

Keywords: deep-buried tunnel; geo-stress characteristics; rock burst prediction; in situ measurement; numerical simulation

check for updates

Citation: Xiang, G.; Zhang, X.; Wang, S.; Wu, S.; Pan, X.; Xu, D. Stress Characteristics and Rock Burst Prediction of the Xuefeng Mountain No.1 Tunnel: On-Site and Numerical Investigations. *Sustainability* **2024**, *16*, 10904. https://doi.org/10.3390/su162410904

Academic Editor: Minghua Huang

Received: 16 October 2024
Revised: 9 December 2024
Accepted: 10 December 2024
Published: 12 December 2024

Copyright: © 2024 by the authors. Licensee MDPI, Basel, Switzerland. This article is an open access article distributed under the terms and conditions of the Creative Commons Attribution (CC BY) license (https://creativecommons.org/licenses/by/4.0/).

1. Introduction

Rock burst is a complex geological and mechanical phenomenon influenced by various factors such as geo-stress conditions, rock properties, excavation methods, and environmental conditions [1–3]. With the increasing scale and complexity of modern engineering constructions, deep-buried tunnels often encounter significant geological challenges, including large deformation of soft rocks, sudden water and mud bursts, rock bursts, etc. Among these, rock bursts are one of particularly serious and unpredictable geological disaster phenomena [4]. Rock bursts generally occur during the construction of deep-buried and highly-stressed tunnels. Excavation and unloading effects induce uneven internal forces within the hard and brittle surrounding rock masses, resulting in the sudden release of accumulated elastic strain energy in rock masses. This release precipitates various dynamic

instabilities such as rock mass loosening, detachment, and jetting, posing significant risks to the safety of operators, equipment, and the construction environment [5–7]. Therefore, it is of great significance to ensure the safety of tunnel construction by evaluating the rock burst failure and risk based on the geo-stress characteristics of deep-buried and highly-stressed surrounding rock masses.

The high geo-stress status of surrounding rock masses is a primary cause of rock bursts in tunnels. Understanding their initial stress status and distributions in tunnels and underground engineering is fundamental in analyzing the prevention and control of rock burst disasters in complex engineering environments [8–10]. The geo-stress of surrounding rock masses in tunnels refers to the stress state acting on various points inside the rock mass, including the horizontal and vertical stress components. Its magnitude and distribution significantly impact the deformation, fracture, and stability of surrounding rock masses in tunnels [11–13]. Ren et al. [14] obtained the geo-stress distribution characteristics of surrounding rock masses in tunnels with complex geological conditions through inversion analysis integrated with multiple regression functions. Meng et al. [15] discussed the initial ground stress field in the rock burst zone based on the lateral pressure coefficient by the secondary inversion analysis. Tang et al. [16] determined the distribution pattern of the ground stress field by observing and analyzing the geological structures of rock salt deposits. You et al. [17] investigated the initial geo-stress distribution of surrounding rock masses in the Daping Mountain Highway Tunnel and found that their initial geo-stress distribution was influenced by multiple factors due to complex geological conditions. For the evaluation of rock bursts in highly stressed surrounding rock masses, Liu et al. [18] conducted experimental research on the strength, deformation, failure, and energy evolution characteristics of rock burst failure in granite under high confining pressure. They found that high confining pressure increased the strength and deformability of granite samples. Peng et al. [19] proposed a calculation method for the release of strain energy in prestressed rock excavation, concluding that rock burst failure in deep-buried tunnel models resulted from strain caused by tangential stress concentration and peeling caused by normal stress release. Duan et al. [20] analyzed the deformation, failure mode, and strain energy evolution of granite, concluding that a higher unloading rate might induce severe failure and that uneven rock deformation leads to strain rupture and fragment ejection. Li et al. [21] used a self-developed rock burst experimental system to reveal the energy evolution characteristics of rock bursts and the relationship between rock burst intensity and their excess energy release rate. All these studies indicate that the stress characteristics of deep-buried tunnels are crucial parameters reflecting the risk of rock bursts. However, due to variations in the buried depth of tunnels and the complexity of geological conditions and structural characteristics, the quantitative relationship between the geo-stress levels and rock burst disasters still requires further studies.

It is well known that rock bursts not only present significant safety hazards to tunnel engineering but also affect the construction progress and tunnel quality [22]. Studies utilizing indoor scaled model experiments have shed light on the mechanism underlying rock bursts. Sun et al. [23] investigated how bedding angles influenced rock burst tendencies in surrounding rock masses; Feng et al. [24] elucidated the microseismic evolution laws and mechanism governing rock burst incubation induced by various construction methods across different rock layers; Li et al. [25] analyzed the brittle failure characteristics of surrounding rock masses by comprehensive analysis, particularly through large-scale rock burst experiments under high geo-stress conditions (the lateral pressure coefficient $\lambda = 2$). Numerical simulations have similarly played a crucial role in unveiling the disaster mechanism associated with rock burst evolution in tunnels [26–28]. Huang et al. [29] simulated rock fracture processes under different confining pressures using the discrete element method, and discussed the granite fracture mechanism and their geometric implications; Qian et al. [30] employed the three-dimensional discrete element method to investigate spontaneous static and dynamic state transition and triggering mechanism of strain-induced rock bursts; Manouchehrian and Cai [31] employed a heterogeneous Abaqus 2D explicit program to

simulate the dynamic rock failure in deep tunnels, confirming the role of nearby weak planes as a critical factor in rock burst occurrence. In terms of rock burst prediction [32,33], researchers have proposed various methods. Yang et al. [34] introduced an energy discrimination index based on rock burst event energy release to assess the probability and severity of such events; Afraei et al. [35] developed an intelligent classification model to predict rock bursts by identifying important predictive variables; Wang et al. [36] proposed a rock burst evaluation method based on interval fuzzy comprehensive evaluation techniques. Although these existing researches provide valuable insights into the mechanism and patterns of rock bursts in tunnels, current research remains primarily exploratory, especially concerning the evolution and prediction of rock bursts in deep-buried tunnels with high geo-stress and complex geological conditions.

Taking the Xuefeng Mountain No.1 Tunnel as the research background, this study presented a rock burst prediction method by combining on-site geo-stress measurements and coupling finite-discrete numerical simulation. Moreover, since rock bursts were significantly determined by the lithology and buried depth of rock masses, the evolution process and potential disaster risk of rock bursts in surrounding rock masses buried at different depths and possessed different lithologies (including granite, slate, and sandstone) were evaluated following the stress–strength ratio criterion and the energy method.

2. Xuefeng Mountain No.1 Tunnel

2.1. Project Overview

The Xuefeng Mountain No.1 Tunnel was a significant component of the high-speed railway line connecting Shanghai to Kunming. It was located within Longhui and Xupu Counties in Hunan Province, China. As shown in Figure 1, the tunnel extended from mileage markers DK243+255 to DK254+925, encompassing a total length of 11,670 m. This tunnel was a critical project within the Hunan section of the Changsha–Kunming Railway Passenger Dedicated Line, designed to support a travel speed of 350 km/h. With a maximum buried depth of approximately 800 m, the tunnel adheres to stringent standards for passenger-dedicated lines.

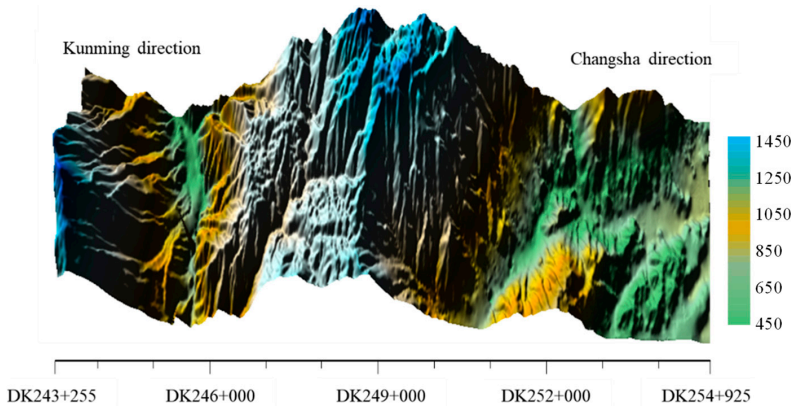


Figure 1. Geological map of the Xuefeng Mountain area.

2.2. Regional Geological Structure

It was well known that rock bursts were closely related to the occurrences of faults and joint structures. When the excavation face was parallel to the direction of fractures or joints, it was extremely easy to trigger a rock burst. It was very necessary to intuitively anticipate what was required to start a survey since rock bursts were not only significantly controlled by the lithology and buried depth of rock masses but also closely related to the spatial distribution of structural planes like faults, joints, and stratigraphic interfaces. Figure 2 illustrates the longitudinal section of the Xuefeng Mountain No.1 Tunnel. It could be found that the Xuefeng Mountain No.1 Tunnel was deep-buried and highly stressed and exhibited varying structural forms at different sections. The stratigraphic distribution was approximately inclined vertically on the whole. An anticline structure was presented near

the Shishui pit at the entrance of the tunnel, and another anticline structure was located in the Jixiang Village at the exit. Except for these two anticlines, most of the rock layers in the remaining parts exhibited monoclinic structures, usually tilting westward and slightly northwest. Their inclination angle ranged from 30° to 70°. It was clear that the excavation face was parallel to the expanding direction of the strata, which meant that there would be a high probability of rock bursts occurring.

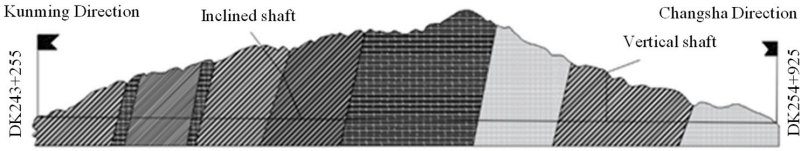


Figure 2. Longitudinal section of the tunnel.

The regional geological map is presented in Figure 3. It could be found that there were strong interactions between tectonic plates. The geological structure near the tunnel entrance (from DK246+890 to DK249+910) was manifested as an anticline structure characterized by a downward slope on the north side and a slight uplift on the south side. This anticline structure was mainly formed by the upward arching of the strata under compression, which usually indicated that the area had experienced a certain degree of pressure in geological history. As shown in Figure 2, the geological structure near the tunnel exit (from DK253+875 to DK255+330) was a developed anticline structure with similar extending characteristics to the tunnel entrance. The exposed rock lithology indicated that this part had experienced similar geological pressure environments. The exposed bedrock revealed the presence of magmatic rocks intermixed with the rock formations in this area, which indicated that the geological activity in this area was dramatic.

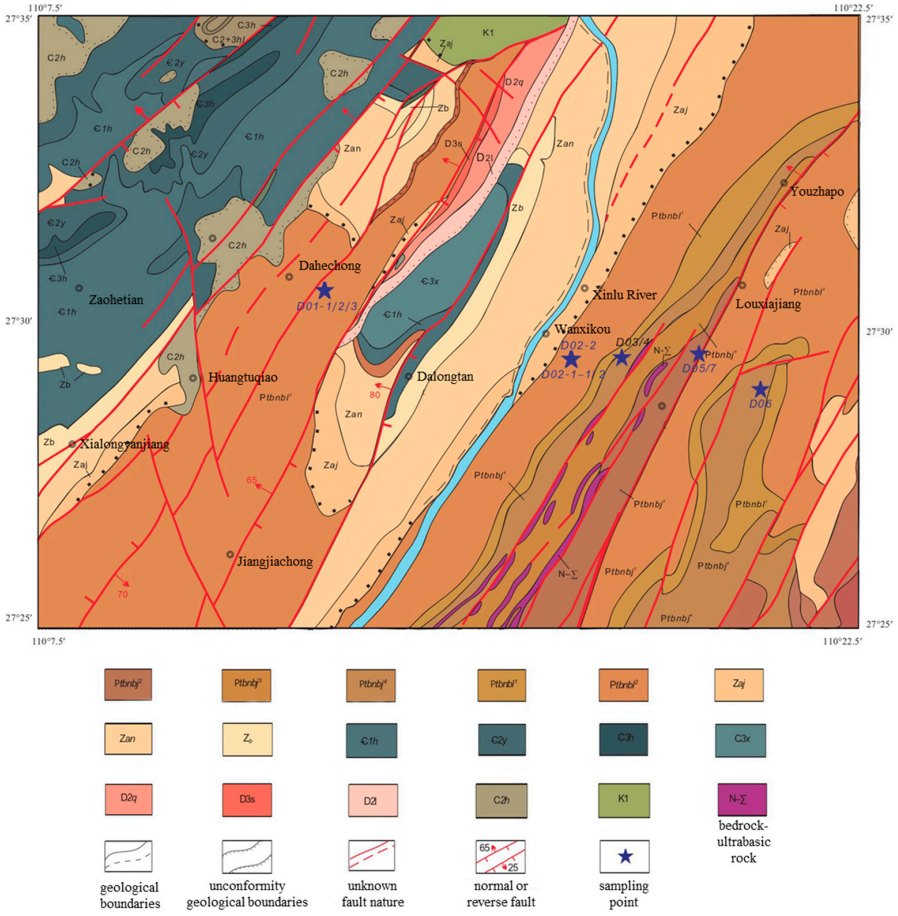


Figure 3. Geological map of the Xuefeng Mountain area (Pu, 2024 [37]).

There were two faults intersected with the tunnel. The F1 fault was a speculative geophysical fault that passed through the main tunnel near DK243+500, trending southeast to south. The F2 fault was located in the eastern part of the Shitan reverse fold, facing northeast and close to DK245+750. It intersected with the tunnel at a large angle and extended in a wavy shape, with a length of over 20 km. The cross-section was generally inclined towards the northwest and twisted towards the northeast, with an inclination angle between 65° and 85°.

2.3. Geological Conditions

The Xuefeng Mountain No.1 Tunnel was situated on the north extension of Xuefeng Mountain, characterized by notably steep terrain. The highest and lowest altitudes were 1453.5 m and 530 m above sea level respectively, resulting in a substantial elevation difference of 923.5 m. The topographic features in this area were complex and variable, featuring interwoven valleys and overlapping mountains. The overall terrain was elevated in the center and gradually flattened towards both ends. The soil thickness of soil near the surface typically ranged from 0.5 to 1.0 m, except in granite areas, where thicker soil layers and abundant vegetation coverage contributed to a more complex surface. Natural slopes mostly ranged from 15° to 35°. Bedrock exposures were more frequent, especially in areas with well-developed gullies or soft and steep areas, as shown in Figures 4 and 5. The surrounding rock mass in the tunnel area had well-developed joints and fissures.



Figure 4. Rocky body in the mountain area.



Figure 5. Rock formation attitude.

The research area along the Xuefeng Mountain No.1 Tunnel exhibited a diverse group of geological layers and extended from the surface to deep strata. Since the excavation face was parallel to the expanding direction of the strata, there might be a high probability of rock bursts occurring. Providing detailed information on the geological structure around the tunnel should thus be very helpful in understanding the rock burst failure. Of course, it also should be noted that this study just employed two-dimensional models to investigate

the stress characteristics and rock burst risk of surrounding rock masses. And since the direction of the tunnel was approximately normal to the expanding direction of the strata, only buried depth and lithology were considered in the study.

The rock composition along the Xuefeng Mountain No.1 Tunnel ranged from the Quaternary to the older geological periods. The surface layer comprised the Quaternary Holocene alluvial layer (Q4Ql+Pl), which was formed by modern river erosion and deposition, consisting of relatively new ground surface sediments. Underlying this stratum was the Upper Pleistocene residual slope layer (Q3Ql+el), which was made up of older eroded materials that were originally part of higher terrain. Beneath these relatively new sedimentary layers lay bedrock layers from the Sinian period, which included the Jinjiadong Formation (Z2j) and the Hongjiang Formation (Z1hj), followed by the Heling Formation (Z1h), the Guanyintian Formation (Z1g), and various members of the Changtan Formation (Z1c3, Z1c2, Z1c1). These formations chronicled the region's ancient geological history and structural evolution. Further geological exploration revealed the presence of the Mobin and Tianjin Formations, which belonged to the Qingbaikou system. These formations were further identified sequentially as the Qbmb2 second formation, Qbmb1 first formation, Qbt4 fourth formation, Qbt2 second formation, and Qbt1 first formation. Additionally, the Shiqiaopu Formation (QbS) and the Jixian Plain Formation (Jxb) were integral components of this intricate geological structure.

2.4. Geological Hazard Risk

The Xuefeng Mountain No.1 Tunnel had a total length of 11,670 m, traveling through various geological conditions. Specifically, it included 1108.7 m of Class V surrounding rock (accounting for 9.5%), 3384.3 m of Class IV surrounding rock (29%), 5356.5 m of Class III surrounding rock (45.9%), and 1820.5 m of Class II surrounding rock (15.6%). Adverse geological conditions within the tunnel area comprise Subsequent Layers, fault fracture zones, rock bursts, geothermal hazards, shallowly buried, sudden water and mud bursts, and karst. Figure 6 presents a typical rock burst incident located at DK249+100 with a buried depth of 751 m. When the excavation of debris in the tunnel was completed and the workers were preparing to carry out drilling construction, there was suddenly a sound coming from the right side wall of the palm face, which was brittle and made the sound of whips and cannons. Then, the arch waist of the right side wall began to crack and peel off. To ensure construction safety, all construction workers evacuated quickly.



(**a**) (**b**) (**c**)

Figure 6. Example of a typical rock burst incident: (**a**) before rock burst; (**b**) rock mass collapse; (**c**) after rock burst.

As an extra-long tunnel, the Xuefeng Mountain No.1 Tunnel was anticipated to experience significant water inflow, intersecting multiple faults, and large anticline structures, such as those in Shishui Pit and Jixiang Village. The geological conditions were extremely complex, posing a high risk during the construction period. A comprehensive analysis of the geological lithology, engineering properties, geological structure, hydrogeology, and special geological features of the tunnel revealed that 55% of the tunnel was prone to collapse, sudden water influx, and large deformation, categorizing it initially at a high-

risk level. Notably, rock burst disasters were prevalent in 25% of the Xuefeng Mountain No.1 Tunnel, characterized by substantial destructive potential, with most initial risk levels classified as extremely high. This phenomenon was attributed to the predominance of granite in Classes II and III surrounding rock masses, which was relatively hard, had a high integrity coefficient, and fulfilled the lithological and structural conditions conducive to rock bursts. Furthermore, the structural stress in this area was high, and groundwater levels were low, which further increased the stress conditions, thereby elevating the probability of rock burst occurrences. The risks within the mileage range of the Xuefeng Mountain No.1 Tunnel are shown in Table 1. It should be noted that these repeated mileage in the right column did not mean that they were superfluous. Due to the complex geological conditions in the tunnel, the risk events near the same mileage were not uniform. Therefore, the mileage with different risk characteristics possessed a certain repeatability.

Table 1. Risk list of Xuefeng Mountain No.1 Tunnel.

ID	Risk Events	Reasons for Risk Generation	Risk Source	Tunnel Sections
1	Sudden water (mud, stone)	(1) Fractured fault zone; (2) Unconformity contact zone of strata; (3) Isolated aquifer	G	DK246+500~DK248+500
2	Landslide	(1) Surrounding rock grade; (2) Fractured fault zone; (3) Rock occurrence, Interlayer bonding force; (4) The occurrence and structural mechanical properties of joints and other structural planes	G	DK248+075~DK248+125 DK248+450~DK248+550 DK253+375~DK253+850
3	Rock burst	(1) The buried depth of the tunnel and the rock hardness were relatively high; (2) Ground stress, direction, and magnitude of principal stress	G	DK245+250~DK245+600 DK246+925~DK247+200 DK249+325~DK250+925
4	Large deformation	(1) Structure character of rock mass; (2) Lithology and weathering degree; (3) Ground stress, direction, and magnitude of principal stress	G	DK247+150~DK248+150 DK249+150~DK249+250 DK251+750~DK252+650
5	Radioactivity	(1) Acidic magmatic rocks	G	DK246+500~DK248+500
6	Instability of the entrance	(1) Soil properties and the thickness of soil layers; (2) Weathering degree and thickness of rock formation; (3) Special rock and soil; (4) Unfavorable geology; (5) High and steep slope, solitary stone	G	DK243+550, DK245+750 DK252+010, DK252+110 DK253+325, DK253+900
7	Surface water loss	(1) The connectivity between surface water and groundwater; (2) Groundwater level; (3) Landforms	G	DK247+113, DK254+026
8	Environmental erosion	(1) Groundwater quality; (2) Groundwater circulation conditions	G	DK245+766, DK247+113

Note: G—Geological factors.

3. Analysis of Geo-Stress Characteristics

3.1. On-Site Geo-Stress Measurement Method

The hole-drilling method is an efficient technique for on-site geo-stress measurement by using specific instruments. This method is particularly suitable for situations that require high-precise measurement of geo-stress in mining, tunnel construction, or other underground engineering. Its basic measurement workflow can commonly be divided into five steps, including selection of measuring points, operations of drilling holes, installation of measuring equipment, release of geo-stress, and data recording and analysis. Among them, the measuring equipment installed in the boreholes commonly includes stress gauges, tension gauges, etc. The dependability of whether the measuring equipment is working properly can be judged by a fixed ratio curve obtained from the indoor biaxial tests on core samples since a fixed ratio test not only provides information about the physical properties

of rocks (such as the elastic modulus and Poisson's ratio) but more importantly presents their mechanical behaviors when subjected to external loadings. The release method of geo-stress in underground rock masses can be realized by blasting, hydraulic, or other appropriate techniques. Moreover, statistical processing and analysis are crucial when conducting multiple measurements, as they can help us minimize errors and effectively organize data. Through this analysis, the magnitude and dip angle of the maximum, intermediate, and minimum principal stresses can be accurately determined, thereby better understanding the structure and properties of the studied object. When implementing on-site geo-stress measurement in the Xuefeng Mountain No.1 Tunnel, a CSIROHID digital hollow inclusion strain gauge shown in Figure 7 was employed to measure the geo-stresses of rock mass inside the boreholes, which was composed of a hollow package structure design, built-in sensors, and a data acquisition system. Install rods, balancers, and mercury locators were used to ensure that measuring equipment such as tension gauges could be accurately placed in the predetermined position and remain stable during operation. The combination of a biaxial testing chamber and a manual hydraulic pump was applied to measure rock stress and strain under controlled conditions, thereby determining the elastic modulus and Poisson's ratio of core samples.



Figure 7. On-site geo-stress measurement devices: (**a**) digital hollow inclusion strain gauge; (**b**) data collection and transmission equipment; (**c**) installed rods; (**d**) balancers; (**e**) mercury locators; (**f**) biaxial testing chamber; (**g**) manual hydraulic pump.

3.2. Scheme Design of On-Site Measurement

The on-site geo-stress measurement of surrounding rock masses enables accurate determination of the magnitude and inclination angle of the maximum, middle, and minimum principal stresses, thereby facilitating a better understanding of the structure and properties of the tunnel's surrounding rock. According to the design drawings and geological exploration report of the Xuefeng Mountain No.1 Tunnel, different typical sections were selected to investigate the initial geo-stress distribution characteristics and rock burst risk of surrounding rock masses, three typical on-site measurement points with different lithologies, buried at depths of 600 m, 700 m, and 800 m and positioned approximately 5000 m, 6450 m, and 3820 m from the tunnel entrance were selected for on-site geo-stress measurements and discrete-continuous coupled numerical analyses, as shown in Figure 8. These sections covered the entire tunnel and included areas with varying geological conditions. The determination of this experimental scheme was based on the following considerations: (1) The lithology of surrounding rock masses near these selected measurement points was the same and uniform, and the distribution of geo-stress did not change significantly. (2) The on-site geo-stress measurement aimed to give a reference to the numeric inversion of geostress although one-point data could result in limited inversion accuracy. (3) The cost of in-situ stress measurement was expensive and these measurement activities also came with certain risks. Boreholes were strategically arranged at measurement points and equipped with stress gauges to measure maximum, intermediate, and minimum principal stresses of surrounding rock masses, along with directional and inclination data. Detailed coordinates of measurement points and the thickness of overburdened rocks are provided in Table 2. The on-site geo-stress measurement at these points utilized the drilling core stress relief method by employing a CSIROHID cell digital hollow enclosure stress detector. The maximum response stress of this device could be up to 100 MPa with an accuracy of ±10 ppm. The full scale of the strain gauge was 10 mm. The diameter of large drilling cores was 100–150 mm, and the diameter of casing drilling cores was 38 mm. The elastic modulus and Poisson's ratio of the rock mass were determined by confining pressure calibration tests to the sampled rock core.

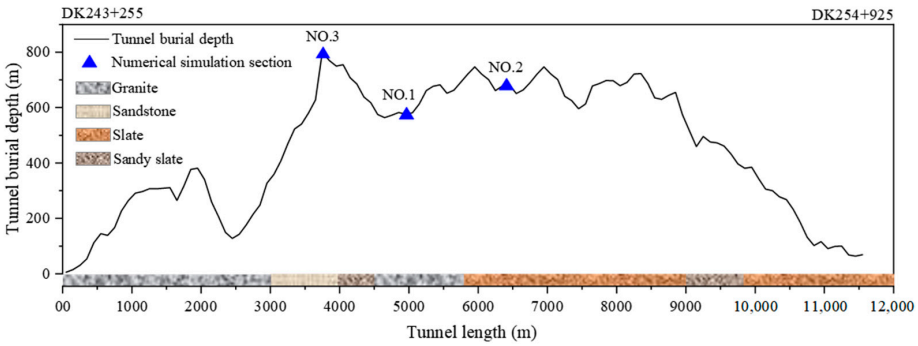


Figure 8. The location of on-site measurement points along the tunnel.

Table 2. Detailed information on measurement points and overburdened rocks.

Point ID	Mileage	Buried Depth (m)	Drilling Location	Azimuth Angle (°)	Inclination Angle (°)
No.1	DK250+850	600	spandrel	262°	3°
No.2	DK249+950	700	spandrel	271°	3°
No.3	DK246+750	800	spandrel	251°	2°

Generally, drilling operations and recording stress data in geological exploration and stress measurement were key steps in understanding the underground rock mass structure and mechanical properties. By using strain gauges and hollow enclosure stress detectors, important data including the stress state and deformation characteristics of rock masses

could be obtained. Figure 9 illustrates the process of on-site measurement. When began drilling, the stress values measured by strain gauges within the first 0.15 m of the borehole casing were relatively small. This was because the stress gauge had not fully entered its most sensitive measurement range. As the drilling depth increased, the stress values recorded by the strain gauge increased gradually. This change indicated that the drilling was just approaching the installation depth of the hollow core package stress gauge, and the deformation of the drilling wall was becoming more pronounced. When the drilling depth reached 0.15–0.30 m, the stress values increased rapidly and tended to be stable, which indicated that the stress gauge had been installed precisely. Then, the stress began to be relieved and the stress state of the surrounding rock masses was recorded. These operations were the critical stage for geo-stress measurement. To ensure the acquisition of representative samples and meet the needs of stress measurement, the design of geo-stress measurement boreholes should consider factors such as drilling depth and diameter. By systematically measuring each position, recording the data, and subsequently processing and analyzing the collected information (including data verification and calculation), the accuracy and reliability of the measured results were evaluated, and the stress distribution characteristics of these surrounding rock masses were analyzed.



Figure 9. On-site measurement: (**a**) drilling large hole; (**b**) completed large hole; (**c**) core samples from the large hole; (**d**) drilling casing hole; (**e**) stress detector installed into holes; (**f**) measurement devices installed; (**g**) core desynchronization testing; (**h**) dislodged casing core samples; (**i**) calibration of core extraction rate.

After the on-site measurement was completed, some principle findings of these measurement points were as follows: For the No.1 measurement point, the core samples taken in the large hole were relatively complete with an average length of 0.37 m, of which 60% of the core samples exceeded 0.30 m, while the length of the core samples within the casing hole was 0.32 m. For the No.2 measurement point, the integrity of the core samples was more complete with an average length of 0.32 m, of which 50% of the core samples exceeded 0.30 m. For the No.3 measurement point, the integrity of the core samples was similarly more complete with the length of the core samples greater than 0.30 m. On the whole, these findings indicated that the integrity of surrounding rock masses disclosed by these three measurement points was good, and the results of the drilling length and the stress relief testing were satisfied ideally.

3.3. Data Analysis of Geo-Stress Measurement

By releasing rock stress and collecting and transmitting data from strain gauges, the measured data are input into a user-developed simple Python calculation program that could help us draw the stress relief curves based on the measured data automatically. The corresponding stress relief curves were presented as shown in Figure 10. The optimal stress test results were achieved through casing measurement, revealing a notable regularity across each curve set. This consistency in curve variations aligns closely with the theoretical analysis of stress relief process changes, affirming the reliability of the measurement results. Then, the testing data were imported into the user-developed analysis program during stress relief testing and rock characteristic testing. The on-site geo-stress measurement results of surrounding rock masses at different sections of the tunnel are presented in Tables 3 and 4, where x, y, and z denoted the directions of the tunnel cross-section and tunnel axis and the direction perpendicular to the ground. It could be found that the maximum and intermediate principal stresses were approximately distributed horizontally while the minimum principal stress was distributed vertically.

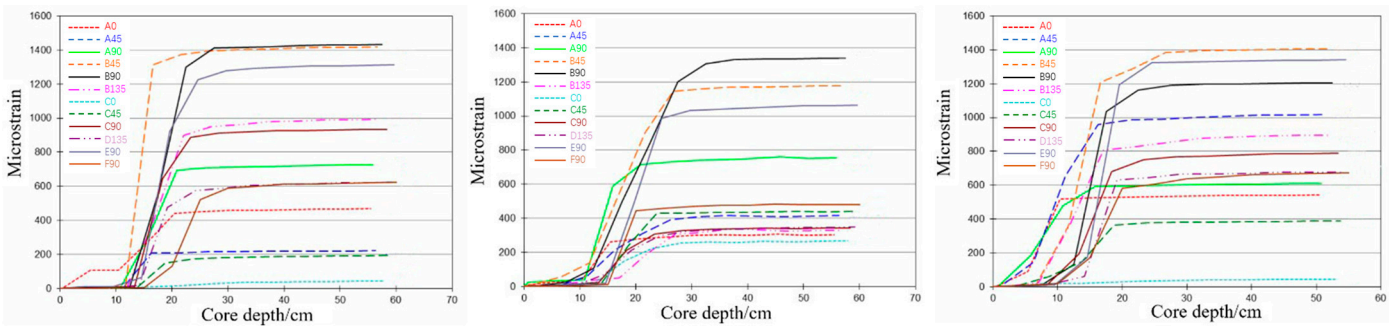


Figure 10. The microstrain output curve of the stress detector during the core testing process: (**a**) buried depth of 600 m; (**b**) buried depth of 700 m; (**c**) buried depth of 800 m.

Table 3. Results of geo-stress testing.

Point ID	Maximum Principal Stress σ_1			Intermediate Principal Stress σ_2			Minimum Principal Stress σ_3		
	Value (MPa)	Direction (°)	Dip Angle (°)	Value (MPa)	Direction (°)	Dip Angle (°)	Value (MPa)	Direction (°)	Dip Angle (°)
No.1	31.9	241	2	20.2	351	20	16.5	125	71
No.2	33.7	216	10	21.3	302	23	18.6	102	69
No.3	37.7	227	18	26.2	323	18	19.1	96	64

Table 4. Calculation results of stress components for rock masses.

Point ID	Buried Depth (m)	Stress Component (MPa)					
		σ_x	σ_y	σ_z	τ_{xy}	τ_{yz}	τ_{zx}
No.1	600	26.4	24.7	17.0	5.7	−1.3	0.4
No.2	700	29.0	25.1	19.2	5.5	−1.6	−0.5
No.3	800	31.0	30.5	21.5	3.7	3.4	2.2

4. Simulation and Prediction of Rock Bursts

4.1. Analysis of Geo-Stress Inversion

The process of back regression analysis on the initial ground stress field of Xuefeng Mountain No.1 Tunnel, utilizing stress relief method test results, can be outlined in several steps as shown in Figure 11.

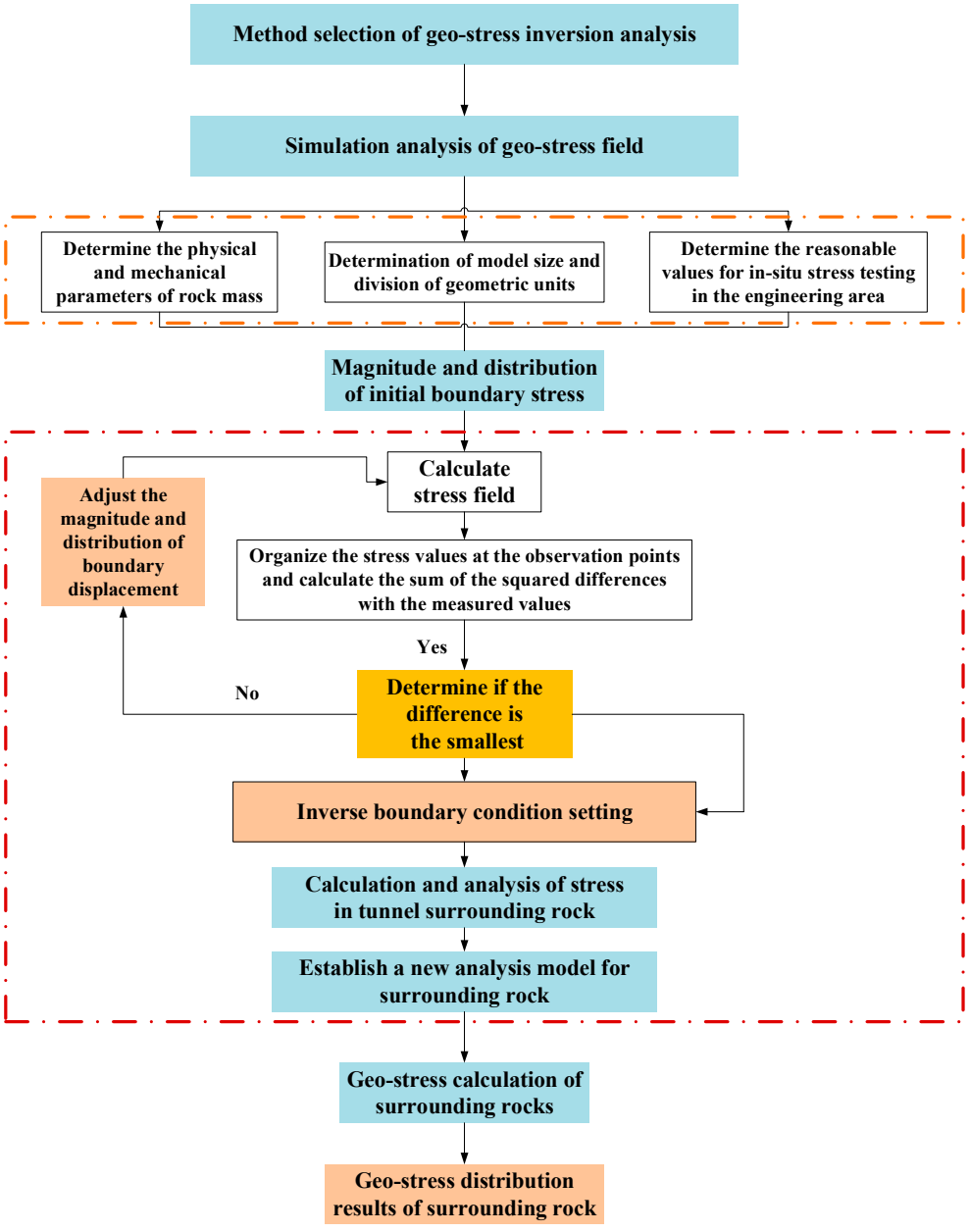


Figure 11. Flow chart of back regression analysis on the initial ground stress field.

(1) Initially, a finite element model of the calculation area was established based on the geological engineering survey.

(2) The main factors affecting the initial geo-stress field of the Xuefeng Mountain No.1 Tunnel were identified through a combination of on-site stress relief testing and geological mechanics analysis, incorporating these as variables of interest. Specifically, finite element simulation was conducted to obtain the stress values at known measurement points. Subsequently, a multiple regression equation was formulated, correlating calculated stress values with those measured at these established points.

(3) Employing the principle of least squares, the optimal coefficients for each variable (undetermined factor) in the multiple regression equation were determined by minimizing the sum of squared residuals. This process could facilitate the calculation of the initial geo-stress field of surrounding rock masses.

Since this study just employed two-dimensional models to investigate the geo-stress characteristics and rock burst risk of surrounding rock masses in deeply buried tunnels, the whole model was supposed to be within the same stratum. Meanwhile, for tracking the fracture evolution induced by the excavation unloading in surrounding rock masses, the disturbance range of surrounding rock masses induced by unloading in this study was considered to exceed three times the tunnel size [38,39]. Accordingly, the model in this study was designed with X and Z scales set at 120 m. The excavation section was characterized by an equivalent circular radius of 7.15 m and an excavation influence zone extending five times the tunnel size was considered. For the geo-stress inversion analysis, all model zones were discretized using the triangular mesh with minimum and maximum sizes of 1.0 m and 5.0 m. The material properties of surrounding rock masses and the overlying layers were derived from geological data and indoor measurements and calibration, which could ensure the representation of real geological conditions. The inversion calculation model is shown in Figure 12 and the physical and mechanical parameters of rock mass are listed in Table 5.

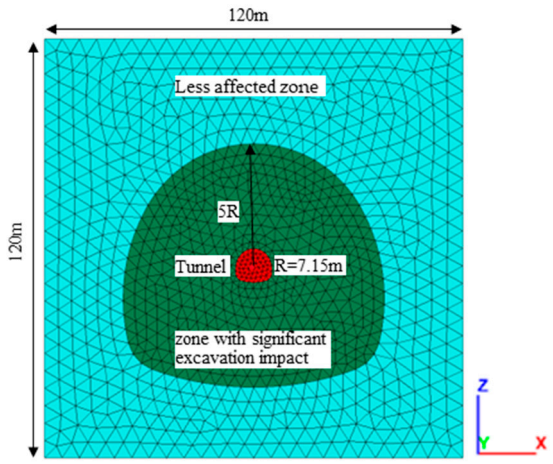


Figure 12. Calculation model of ground–stress inversion.

Table 5. Physical and mechanical parameters of rock mass.

Rock Mass Type	Buried Depth (m)	Density (g/cm^3)	Unit Weight (kN·m^{-3})	Elastic Modulus (GPa)	Poisson's Ratio	Internal Friction Angle (°)	Cohesion (MPa)	Tensile Strength (MPa)
granite	600	2800	28.0	48.1	0.27	50	1.8	5.5
slate	800	2600	26.0	45.5	0.22	48	1.6	4.0
sandstone	700	2500	24.0	41.8	0.35	30	0.3	2.5

The accurate simulation and analysis of the initial geo-stress field are crucial for ensuring structural safety and effectiveness in geological engineering and tunnel design. It is known that the initial ground stress field primarily consists of gravitational and

structural stress components. Therefore, to ensure the correctness of numerical simulations, a constant gravitational acceleration of 9.81 m/s^2 was applied for the finite element model, in which zero displacement constraints were applied to the model's sides and bottom. The overburden depths of the model were set at 600, 700, and 800 m, respectively. To simulate the compressive tectonic movements along the X and Y axes, unit displacements were applied in these directions after establishing the initial gravitational stress field. The rock mass properties were represented as an ideal elastic medium, allowing for the conversion of displacement constraints reference values based on the linear relationship between inversed and measured stresses. Given the interdependence of force changes in different directions, a multiple regression algorithm optimizes the displacement constraint values. The inversion results of the initial ground stress field along a typical section of the Xuefeng Mountain No.1 Tunnel are depicted in Figure 13. It could be found that the initial vertical geo-stress of these models with different buried depths had a similar layered distribution. The deeper the buried depth, the higher the vertical geo-stress. Table 6 compares measured geo-stress values at three stress relief drilling points with results from inverse regression calculations, where x, y, and z denoted the directions of the tunnel cross-section and tunnel axis and the direction perpendicular to the ground. The similarity between inversed and measured values, with errors controlled within 16%, indicated a consistent trend and pattern, accurately reflecting the stress state of surrounding rock masses. This well underscored the reasonableness and reliability of the ground stress field obtained through inverse regression in the Xuefeng Mountain tunnel area.

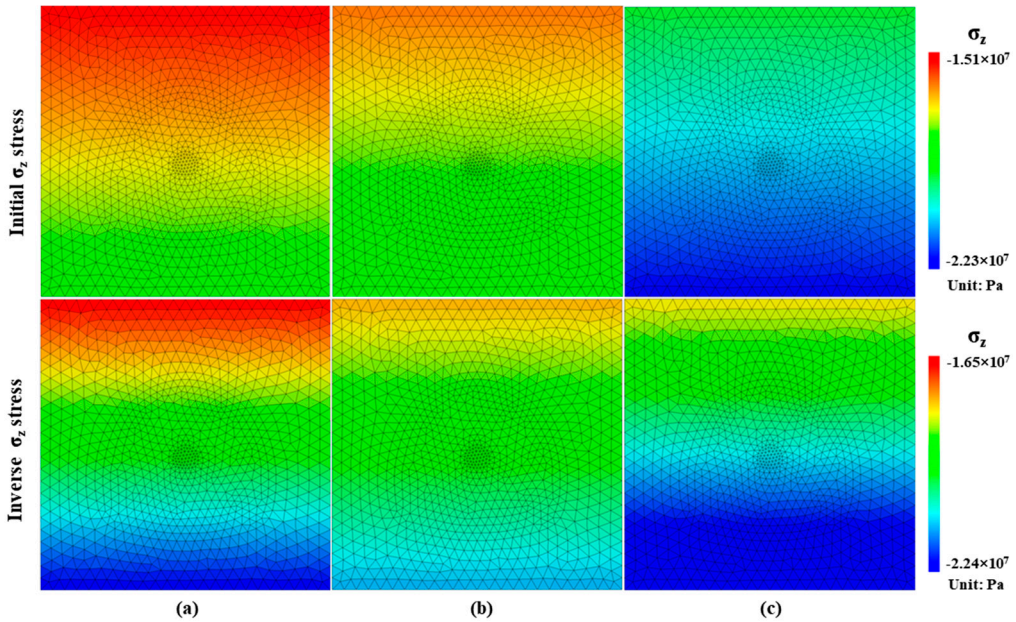


Figure 13. Geo−stress simulation: (**a**) buried at 600 m; (**b**) buried at 700 m; (**c**) buried at 800 m.

Table 6. Comparison between calculated and measured values.

Point ID	Buried Depth (m)	Actual Measured Value (MPa)			Numerical Simulated Value (MPa)		
		σ_x	σ_y	σ_z	σ_x	σ_y	σ_z
No.1	600	26.4	24.7	17.0	27.5	22.1	19.6
No.2	700	29.0	25.1	19.2	29.7	26.8	20.1
No.3	800	31.0	30.5	21.5	32.6	31.7	21.3

4.2. Coupling Calculation Model

This study also employed discrete and continuous coupling simulation technology to analyze the rock burst evolution of surrounding rock masses in the Xuefeng Mountain No.1

Tunnel. The calculation model dimensions were aligned with the previously mentioned stress inversion model. Considering that rock burst failure constitutes a large deformation problem, a particle discrete element model was designed using Particle Flow Code (PFC) for the surrounding rock masses within the influence range of tunnel excavation. Simultaneously, an elastic-plastic finite difference mesh model created with Flac3D was used for the rock masses outside the influence range, as shown in Figure 14. The size of the excavation influence zone was supposed to be five times the tunnel size. The interaction between the discrete and finite zones was linked by specified triangle interface elements. The discrete model within the influence range was generated using the ball distribution command in batches, comprising 4800 particles with a radius of 0.2–0.4 m. A triangular coupling boundary was established between the continuous and discrete domains within and outside the excavation's influence range. Python language was employed to map this coupling boundary, ensuring that the particle contact force in the discrete domain was accurately transferred to the continuous domain node, and vice versa for the node velocity of the continuous domain to the boundary-controlled domain particles. This methodology could ensure continuous transmission across the coupling boundary between the continuous and discrete domains.

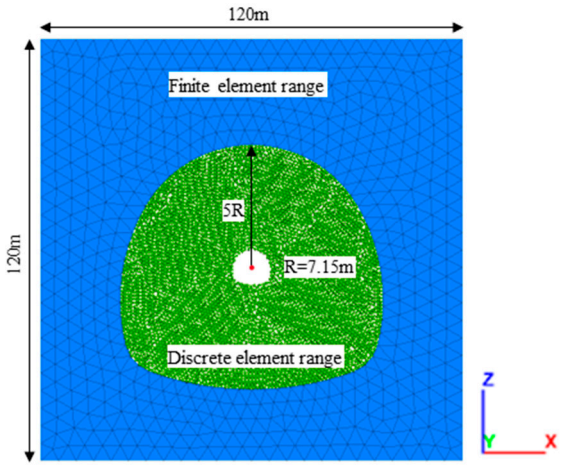


Figure 14. Establishment of the coupling calculation model.

Considering the model represented a local stratigraphic segment, vertical loads were applied to the upper boundary to simulate the pressure of the overlying layer. The magnitude of the load was determined based on different buried depths and geological conditions. Displacement constraints were applied to the left, right, and lower boundaries of the model. To thoroughly analyze the rock burst risk of surrounding rock masses in the Xuefeng Mountain No.1 Tunnel, six potential transverse sections were screened, and the rock burst failure evolution of these sections was simulated. Then, the energy release, crack propagation, and deformation development of surrounding rock masses in the tunnel with different rock types and buried depths were analyzed. These analyses aimed to elucidate the geo-stress disturbance in the surrounding rock masses induced by the tunnel excavation and the possibility of rock burst occurrence. The physical and mechanical parameters utilized for the evolution simulation of the rock burst disaster are consistent with those listed in Table 5. The microscopic parameters for the discrete element model, such as particle size, contact stiffness, and stiffness ratio, are listed in Table 7.

Table 7. Microscopic parameters of discrete particle elements.

Parameters	Description	Rock Mass Type		
		Granite	Slate	Sandstone
ball_kn	Ball normal stiffness (Pa)	2.46×10^{10}	2.05×10^{10}	2.27×10^{10}
ball_ks	Ball shear stiffness (Pa)	2.46×10^{10}	2.05×10^{10}	2.27×10^{10}
ball_fric	Ball friction coefficient	5.7×10^{-1}	5.1×10^{-1}	4×10^{-1}
ball radius	Ball radius	0.2~0.4	0.2~0.4	0.2~0.4
pb_krat	Parallel bond normal/shear stiffness ratio	1.0	1.0	1.0
pb_coh	Parallel bond cohesive strength (Pa)	3×10^{6}	2.8×10^{6}	2.1×10^{6}
pb_ten	Parallel bond tense strength (Pa)	1.5×10^{6}	1.2×10^{6}	1.0×10^{6}
pb_rmul	Parallel bond radius multiplier	9.8×10^{-1}	9.7×10^{-1}	9.8×10^{-1}

4.3. Evolution Simulation of Rock Burst

Following these on-site measured data and the stress inversion results mentioned above, the discrete and continuous coupling simulation for rock burst failure was conducted for the tunnel transverse sections with different buried depths and lithological conditions. Since the spatial layout of the Xuefeng Mountain No.1 Tunnel was a herringbone shape, the depth of the surrounding rock masses possessing the same lithology and geological structure in the tunnel might be different due to location. To investigate the differences in rock burst evolution, the model of the tunnel possessing the same geological conditions and buried at different depths was employed to conduct a comparative analysis by selecting two sections with similar depths. Displacement contours under different operational conditions are illustrated in Figures 15–17. Notably, some model particles had already displayed initial dispersion at 500 calculation steps. When the calculation step reached 2500–4500, sheet-like splitting began, accompanied by particle ejection. After 2500 steps, the model predominantly exhibited block collapse and significant particle ejection, leading to a significant increase in large displacement particles within the model. Particles at the unloading surface appeared as contact failures on the displacement vector map, indicating a greater displacement. The total displacement of the tunnel vault showed a gradual decrease from the rock wall towards the deeper surrounding rock masses. During a rock burst occurrence, the inverted arch, arch foot, and both sides of the arch waist were greatly affected by the release of geo-stress, exhibiting greater vault displacement compared to the tunnel crown. Moreover, as the buried depth increased, the total displacement was more profoundly influenced by initial geo-stress, showing a continuous upward trend. These displacements indicated an increasing trend with calculation steps, demonstrating a left-right asymmetry due to the uneven distribution of the initial geo-stress. Upon comparing the crack generation process across models at varying buried depths, it became evident that, with the increasing geo-stress and computational steps, there was a deepening dispersion of model particles. Subsequently, the connection between the later-stage peeled-off particles and the main model particle fractures resulted in a state of separation. Furthermore, as buried depth increases, the color distinction of the displacement vector distribution map becomes more pronounced. This finding highlights larger absolute differences in particle displacement inside the model, indicating that there should be a greater instability of these surrounding rock masses being subjected. When examining the displacement distribution maps of different types of surrounding rock masses, it was observed that both slate and granite arches exhibited similar patterns of large displacement areas. However, the granite showed a wider radiation area with a great number of particles experiencing significant displacements. Given the superior mechanical properties of granite compared to slate, granite thus should be more susceptible to extensive damage in the event of a rock burst.

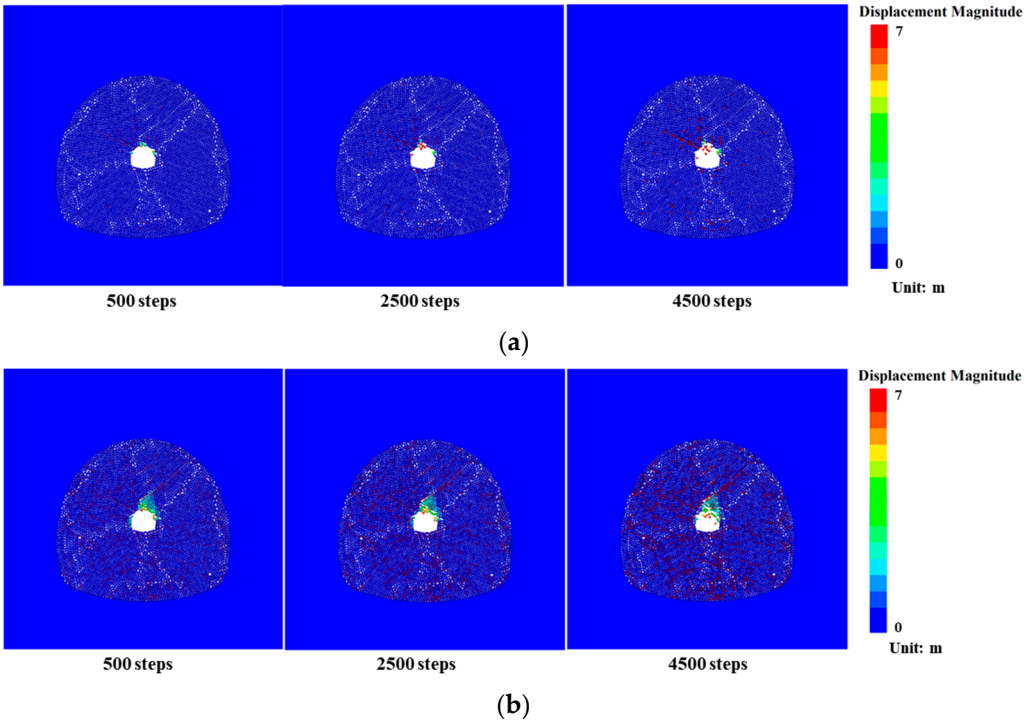


Figure 15. Displacement contour of granite buried at different depths: (**a**) the buried depth was 585 m; (**b**) the buried depth was 600 m.

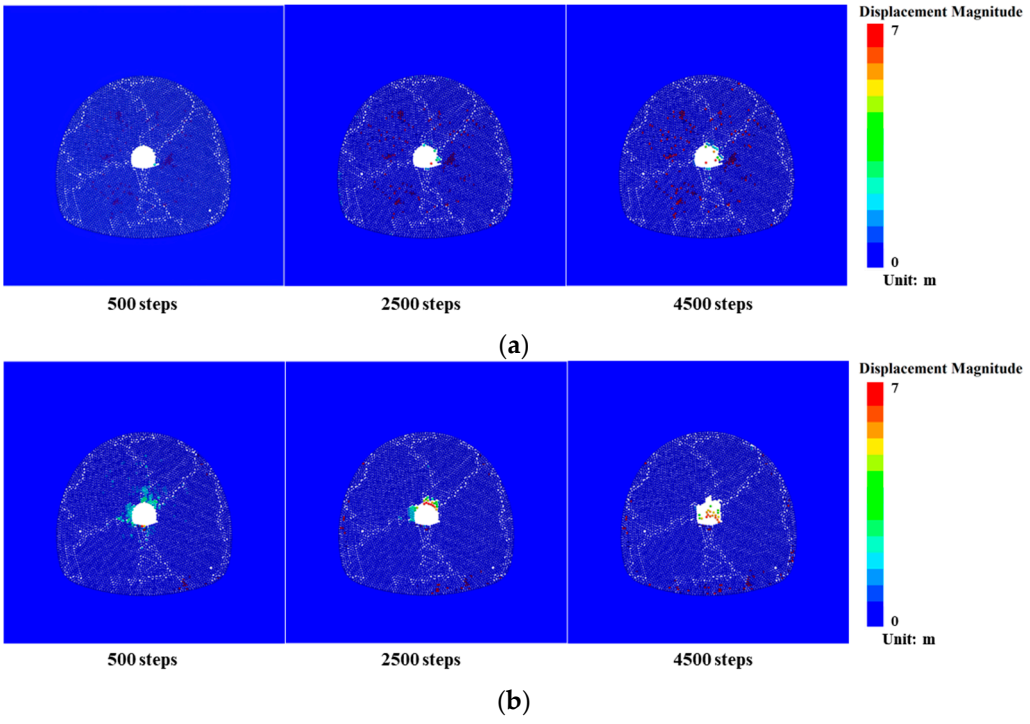
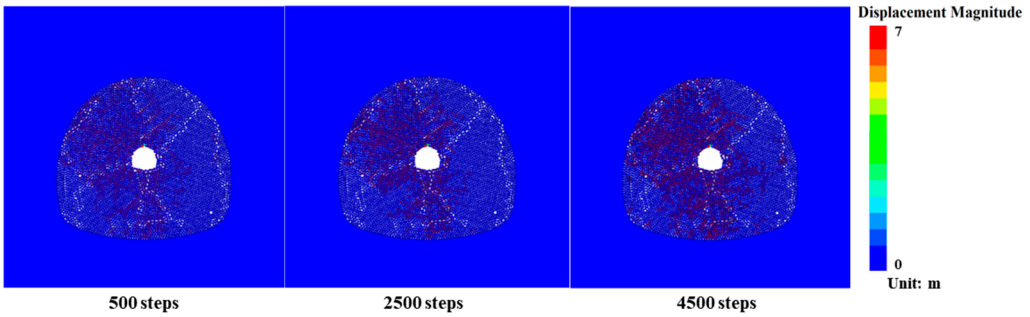
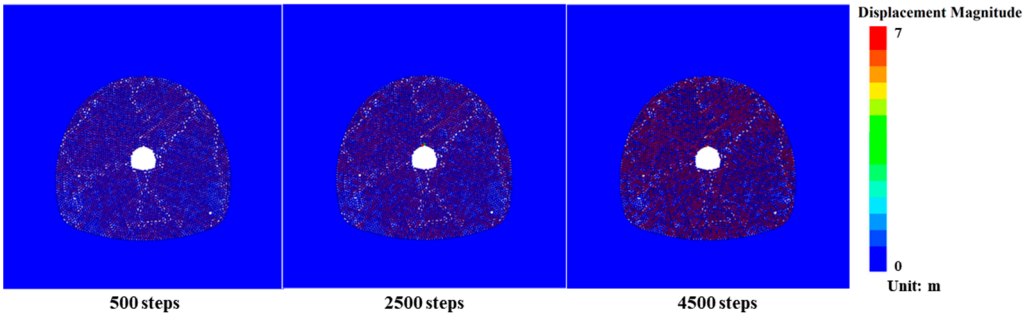


Figure 16. Displacement contour of slate buried at different depths: (**a**) the buried depth was 685 m; (**b**) the buried depth was 700 m.



(**a**)



(**b**)

Figure 17. Displacement contour of sandstone buried at different depths: (**a**) the buried depth was 785 m; (**b**) the buried depth was 800 m.

4.4. Risk Prediction of Rock Burst

The energy method assesses the possibility of rock bursts by analyzing the energy changes during rock deformation and fracture. It utilizes stress–strain curves derived from laboratory experiments to evaluate the potential for rock bursts, taking into account internal rock factors and the energy evolution process of rock masses under external loading. Typically, the probability and intensity of rock bursts can be evaluated through an analysis of the elastic strain energy index of rock masses (usually referred to as W_{et}). This index can be determined as the ratio of stored elastic strain energy to dissipated elastic strain energy as follows:

$$W_{et} = \frac{\phi_{sp}}{\phi_{st}} \quad (1)$$

where ϕ_{sp} is the elastic strain energy and ϕ_{st} is the dissipated strain energy.

The national standard has delineated the specific rock burst risk levels based on the thresholds of the elastic strain energy index. According to these standards, a $W_{et} \geq 5.0$ indicates a severe rock burst risk, W_{et} = 2.0~4.9 suggests a moderate to low-intensity rock burst risk, and a $W_{et} < 2.0$ implies that a rock burst is unlikely to occur. Table 8 presents the rock burst discrimination results for the Xuefeng Mountain No.1 Tunnel. There is a higher probability of severe rock bursts occurring in granite at a depth of 600 m. Granite at a depth of 585 m is categorized as having a moderate rock burst risk. The slate at approximately 700 m is classified as having a weak rock burst risk. Conversely, sandstone is classified as having no rock burst risk. To verify the correctness of the energy method for rock burst prediction, a comparative analysis was conducted with the prediction results obtained using the stress strength ratio criterion. The corresponding discrimination criterion was referenced by the documented research [40].

$$W_b = \frac{\sigma_1}{\sigma_c} \quad (2)$$

where σ_1 is the maximum principal stress of surrounding rock masses; σ_c is the saturated uniaxial compressive strength of rock mass. When $W_b < 0.2$, it indicates the absence of a

rock burst; when $0.2 \leq W_b < 0.3$, a weak rock burst is expected; when $0.3 \leq W_b < 0.55$, it signifies a moderate rock burst; and when $W_b \geq 0.55$, a strong rock burst is anticipated.

Table 8. Rock burst discrimination.

ID of Sample	Lithology	Buried Depth (m)	The Energy Method		The Stress–Strength Ratio Criterion	
			W_{et}	Rock Burst Degree	W_b	Rock Burst Degree
09-ZD-10349	granite	600	5.12	Severe rock burst	0.6	Severe rock burst
09-ZD-10350	granite	585	4.31	Moderate rock burst	0.57	Severe rock burst
09-ZD-10352	slate	700	2.75	Weak rock burst	0.23	Weak rock burst
09-ZD-10354	slate	685	2.35	Weak rock burst	0.27	Weak rock burst
09-ZD-10355	sandstone	800	1.99	No rock burst	1.8	No rock burst
09-ZD-10357	sandstone	785	1.90	No rock burst	1.95	No rock burst

The comparative analysis between the elastic strain energy method and the stress–strength ratio criterion showed that although their predicted conclusions were in good agreement, the evaluation results obtained using the stress–strength ratio criterion were more conservative. The simulated strain energy dissipation process curve shown in Figure 18 illustrates that the release of geo-stress resulted in varying energy dissipation characteristics in surrounding rock masses with different lithologies and buried depths during the tunnel excavation. The energy dissipation for the granite buried at depths of 600 m and 585 m, as well as the slate buried at 700 m, exhibited slow changes and minimal reduction, which indicated a relatively high amount of stored elastic strain energy and an increasing risk of rock bursts. In contrast, the energy dissipation observed in the slate buried at 685 m and the sandstone buried at 785 m and 800 m were more significant, which reduced the potential risk of rock bursts. Further comparative analysis in Table 8 revealed that when the buried depth of the tunnel was similar, the energy dissipation behavior of the slate varied significantly, indirectly reflecting the rock burst sensitivity of the slate to the buried depth.

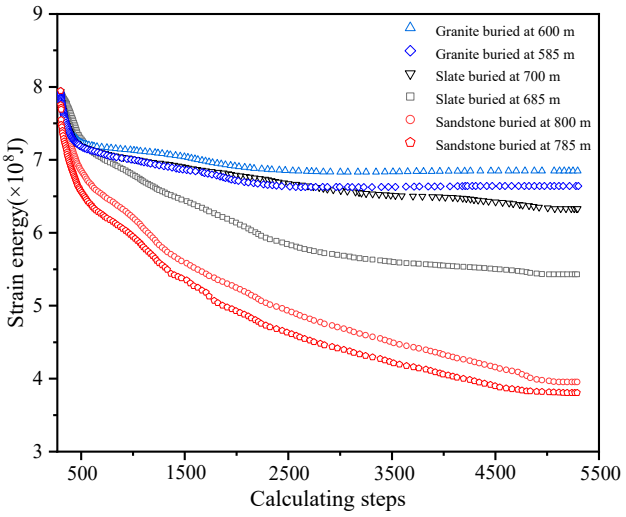


Figure 18. Strain energy dissipation curves of surrounding rock masses with different lithologies and buried depths.

5. Conclusions

The geo-stress distribution characteristics of surrounding rock masses in the deeply buried and highly stressed Xuefeng Mountain No.1 Tunnel were investigated through a combination of on-site geo-stress measurements and discrete-continuous coupled numerical simulations. The evolution process of rock burst failure in different tunnel sections with various buried depths and lithologies was discussed. The risk of rock bursts along this long tunnel was predicted using the stress–strength ratio criterion and the energy method. Some primary conclusions are obtained as follows:

(1) The on-site hole-drilling measurement showed that the maximum horizontal principal stress, intermediate horizontal principal stress, and minimum principal stress of the surrounding rock masses in the Xuefeng Mountain No.1 Tunnel exhibit a nearly linear growth trend as the depth of buried increases, and their maximum and intermediate principal stresses were approximately distributed horizontally while their minimum principal stresses were distributed vertically. The principal stress values on the whole followed the distribution pattern of $\sigma_x > \sigma_y > \sigma_z$ with an average stress exceeding 20 MPa. This distribution indicates that the tunnel was primarily dominated by horizontal tectonic stress.

(2) The inversed initial vertical geo-stress of typical tunnel sections with different buried depths showed a similar layered distribution. The inversed and measured values possessed a consistent trend and pattern with errors within 16%. The phenomenon of rock burst failure in the Xuefeng Mountain No.1 Tunnel was characterized by the sheet-like splitting of rock layers accompanied by the ejection of particles. The areas of stress concentration and elastic deformation energy accumulation were mainly located in the inverted arch of the tunnel. As the tunnel's depth increased, the deformation intensified correspondingly. The inverted arch, arch foot, and both sides of the arch waist of the tunnel were significantly impacted by the release of geo-stress, exhibiting greater displacement compared to the vault. The displacement of the vault in the tunnel showed a gradually decreasing trend from the tunnel outline to the deeper surrounding rock masses. Both slate and granite arches exhibited similar patterns of large displacement areas. However, the granite showed a wider radiation area with a great number of particles experiencing significant displacements. The granite, thus, should be more susceptible to extensive damage in the event of a rock burst given the rock's mechanical properties.

(3) The combination of the stress–strength ratio criterion and the energy method showed that they could offer a more comprehensive explanation of the instability and rock burst failure in tunnel and underground engineering. However, although their predicted conclusions were in good agreement, the evaluation results by the stress–strength ratio criterion were more conservative. When the buried depth of the tunnel was similar, the rock burst of the slate was sensitive to the buried depth.

(4) Although the findings of this study can provide valuable insights into the geo-stress characteristics and rock burst prediction for surrounding rock masses in these deep-buried, highly-stressed tunnel environments, the occurrence of rock bursts has suddenness and uncertain, and the influencing factors that need to be considered are not limited to the buried depth and lithology. The related factors like Fault and joint structures should also be considered. Moreover, there is no clear qualitative and quantitative unified judgment on the problem of rock bursts currently, which is still a global challenge that has not yet been overcome. The task of building the unified rock burst prediction theory and methods is a challenge researchers must overcome if they are to predict the occurrence of rock bursts accurately.

Author Contributions: Conceptualization, G.X.; Funding acquisition, S.W. (Shengnian Wang); Resources, G.X.; Validation, D.X.; Writing—original draft, G.X. and X.Z.; software, X.P.; Writing—review and editing, X.Z., S.W. (Shengnian Wang) and S.W. (Sanyou Wu). All authors have read and agreed to the published version of the manuscript.

Funding: The research was conducted with funding provided by the Key Program of the National Natural Science Foundation of China (Grant No. 42330704) and the National Natural Science Foundation of China (Grant No. 41902282).

Data Availability Statement: The data presented in this study are available on request from the corresponding author.

Conflicts of Interest: The authors declare no conflicts of interest.

References

1. Feng, F.; Li, X.; Luo, L.; Zhao, X.; Chen, S.; Jiang, N.; Huang, W.; Wang, Y. Rockburst Response in Hard Rock Owing to Excavation Unloading of Twin Tunnels at Great Depth. *Bull. Eng. Geol. Environ.* **2021**, *80*, 7613–7631. [CrossRef]
2. Wu, J.; Zhang, X.Y.; Yu, L.Y.; Zhang, L.W.; Wu, T. Rockburst Mechanism of Rock Mass with Structural Planes in Underground Chamber Excavation. *Eng. Fail. Anal.* **2022**, *139*, 106501. [CrossRef]
3. Yang, J.; Yang, X.-G.; Zhou, J.-W.; Liu, Y.; Dong, B.-S.; Li, H.-B. Comparative Study of the Excavation Damage and Rockburst of the Deeply Buried Jinping II Diversion Tunnels Using a TBM and the Drilling-Blasting Method. *Adv. Civ. Eng.* **2020**, *2020*, 8876214. [CrossRef]
4. Zhang, H.; Chen, L.; Chen, S.; Sun, J.; Yang, J. The Spatiotemporal Distribution Law of Microseismic Events and Rockburst Characteristics of the Deeply Buried Tunnel Group. *Energies* **2018**, *11*, 3257. [CrossRef]
5. Chu, Z.; Wu, Z.; Liu, Q.; Liu, B.; Sun, J. Analytical Solution for Lined Circular Tunnels in Deep Viscoelastic Burgers Rock Considering the Longitudinal Discontinuous Excavation and Sequential Installation of Liners. *J. Eng. Mech.* **2021**, *147*, 04021009. [CrossRef]
6. Walton, G.; Gaines, S.; Alejano, L.R. Validity of Continuous-Failure-State Unloading Triaxial Tests as a Means to Estimate the Residual Strength of Rocks. *Chin. J. Rock Mech. Eng.* **2021**, *13*, 717–726. [CrossRef]
7. Feng, F.; Chen, S.; Li, D.; Huang, W.; Peng, K.; Zang, C. Excavation Unloading-induced Fracturing of Hard Rock Containing Different Shapes of Central Holes Affected by Unloading Rates and in Situ Stresses. *Energy Sci. Eng.* **2020**, *8*, 4–27. [CrossRef]
8. Feng, X.; Zhang, C.; Chen, B.; Feng, G.; Zhao, Z.; Ming, H.; Xiao, Y.; Duan, S.; Zhou, H. Dynamical control of rockburst evolution process. *Chin. J. Rock Mech. Eng.* **2012**, *31*, 1983–1997.
9. Zhang, Z.; Zhang, J.; Xu, J.; Luo, C. Study on fracture characteristics and rockburst process of hard sandstone under high ground stresses. *Chin. J. Rock Mech. Eng.* **2024**, *43*, 50–58. [CrossRef]
10. Chen, G.; Li, T.; Zhang, G.; Yin, H.; Zhang, H. Temperature Effect of Rock Burst for Hard Rock in Deep-Buried Tunnel. *Nat. Hazards* **2014**, *72*, 915–926. [CrossRef]
11. Huber, K.; Fuchs, K.; Palmer, J.; Roth, F.; Khakhaev, B.N.; Van-Kin, L.E.; Pevzner, L.A.; Hickman, S.; Moos, D.; Zoback, M.D.; et al. Analysis of Borehole Televiewer Measurements in the Vorotilov Drillhole, Russia—First Results. *Tectonophysics* **1997**, *275*, 261–272. [CrossRef]
12. Chen, Y.; Zuo, J.; Liu, D.; Li, Y.; Wang, Z. Experimental and Numerical Study of Coal-Rock Bimaterial Composite Bodies under Triaxial Compression. *Int. J. Coal Sci. Technol.* **2021**, *8*, 908–924. [CrossRef]
13. Feng, G.L.; Feng, X.T.; Chen, B.; Xiao, Y.X.; Yu, Y. A Microseismic Method for Dynamic Warning of Rockburst Development Processes in Tunnels. *Rock Mech. Rock Eng.* **2015**, *48*, 2061–2076. [CrossRef]
14. Ren, H.; Tan, Z.; Feng, P. Back Analysis of In-Situ Stress under Complicated Geological Conditions Based On Function Superposition of Multiple Regressions. *Eng Technol. Res.* **2017**, *5*, 157–165. [CrossRef] [PubMed]
15. Meng, W.; He, C.; Zhang, J.; Zhou, Z.; Wang, B. Inversion analysis of initial geostress field of rock mass under high temperature and high stress conditions. *Chin. J. Rock Mech. Eng.* **2020**, *39*, 749–760. [CrossRef]
16. Tang, J.; Wang, H.; Li, X.; Xian, X.; Du, Y. Measurement and characteristics of in-situ stress in deep rock salt mine. *Chin. J. Rock Mech. Eng.* **2004**, *23*, 3954–3958.
17. Zhemin, Y.; Jianping, C.; Yongsong, L.; Fang, X. Discussion on Distribution of In-Situ Stress in Highway Tunnel with Great Depth in Daping Mountain. *Chin. J. Undergr. Space Eng.* **2013**, *9*, 231–235.
18. Liu, Z.; Wang, H.; Li, Y.; Wang, X.; Selvadurai, A.P.S. Triaxial Compressive Strength, Failure, and Rockburst Potential of Granite Under High-Stress and Ground-Temperature Coupled Conditions. *Rock Mech. Rock Eng.* **2023**, *56*, 911–932. [CrossRef]
19. Xiao, P.; Li, D.; Zhu, Q. Strain Energy Release and Deep Rock Failure Due to Excavation in Pre-Stressed Rock. *Minerals* **2022**, *12*, 488. [CrossRef]
20. Duan, K.; Ji, Y.; Wu, W.; Kwok, C.Y. Unloading-Induced Failure of Brittle Rock and Implications for Excavation-Induced Strain Burst. *Tunn. Undergr. Space Technol.* **2019**, *84*, 495–506. [CrossRef]
21. Li, J.; Liu, D.; He, M.; Guo, Y.; Li, N.; Zhang, J. Experimental Investigation on Pillar Rockburst of True Triaxial Four-Face Rapid Unloading under High Stress. *Bull. Eng. Geol. Environ.* **2024**, *83*, 125. [CrossRef]
22. Hou, S.; Xie, F.; Tian, S.; Liang, S. Effects of Blasting Vibrations on an Arch in the Jiaohuayu Tunnel Described by Energy Response Spectrum Analysis. *Appl. Sci.* **2022**, *12*, 11395. [CrossRef]
23. Sun, X.; Yuan, J.; Xu, Y.; Ren, C.; Zhao, W.; Zhang, X.; Tian, S. Rockburst Tendency Discrimination of GaoloushanTunnel Based on Multiple Criteria. *Sci. Technol. Eng.* **2021**, *21*, 4621–4626.
24. Feng, X.; Xiao, Y.; Feng, G.; Yao, Z.; Chen, B.; Yang, C.; Su, G. Study on the development process of rockbursts. *Chin. J. Rock Mech. Eng.* **2019**, *38*, 649–673. [CrossRef]
25. Li, T.; Zhong, Y.; Pan, H.; Chen, G. Failure Characteristics Analysis on Physical Model of Rock Burst in High In-Situ Stress Tunnel. *Chin. J. Undergr. Space Eng.* **2019**, *15*, 1639–1645.
26. Jin, H.; Yuan, D.; Zhou, S.; Zhao, D. Short-Term and Long-Term Displacement of Surface and Shield Tunnel in Soft Soil: Field Observations and Numerical Modeling. *Appl. Sci.* **2022**, *12*, 3564. [CrossRef]
27. Choi, Y.-H.; Lee, S.S. Reliability and Efficiency of Metamodel for Numerical Back Analysis of Tunnel Excavation. *Appl. Sci.* **2022**, *12*, 6851. [CrossRef]

28. Wang, J.; Cao, A.; Liu, J.; Wang, H.; Liu, X.; Li, H.; Sun, Y.; Long, Y.; Wu, F. Numerical Simulation of Rock Mass Structure Effect on Tunnel Smooth Blasting Quality: A Case Study. *Appl. Sci.* **2021**, *11*, 10761. [CrossRef]
29. Feng, H.; Tianyong, L.I.; Xiaoye, G.A.O.; Xiang, Y.; Zhi, L.I.N. Study on the Macro-Micro Failure Mechanism of Granite and Its Geometry Effect under the Different Conditions of Confining Pressure by Discrete Element. *J. Coal Sci.* **2019**, *3*, 70. [CrossRef]
30. Qian, Y.; Zhao, C.; Wei, R.; Zhang, R.; Huang, L.; Chen, H. Self-Initiated Static-Dynamic State Transition Behavior and Triggering Mechanism of Strain Rockburst Using Three-Dimensional Discrete Element Method. *Undergr. Space* **2024**, *16*, 143–163. [CrossRef]
31. Manouchehrian, A.; Cai, M. Numerical Modeling of Rockburst near Fault Zones in Deep Tunnels. *Tunn. Undergr. Space Technol.* **2018**, *80*, 164–180. [CrossRef]
32. Wang, J.; Cao, A.; Wu, Z.; Sun, Z.; Lin, X.; Sun, L.; Liu, W.; Liu, X.; Li, H.; Sun, Y.; et al. Dynamic Risk Assessment of Ultra-Shallow-Buried and Large-Span Double-Arch Tunnel Construction. *Appl. Sci.* **2021**, *11*, 11721. [CrossRef]
33. Zhang, S.; Tang, C.; Wang, Y.; Li, J.; Ma, T.; Wang, K. Review on Early Warning Methods for Rockbursts in Tunnel Engineering Based on Microseismic Monitoring. *Appl. Sci.* **2021**, *11*, 10965. [CrossRef]
34. Yang, F.; Zhou, H.; Lu, J.; Zhang, C.; Hu, D. An energy criterion in process of rockburst. *Chin. J. Rock Mech. Eng.* **2015**, *34*, 2706–2714. [CrossRef]
35. Afraei, S.; Shahriar, K.; Madani, S.H. Developing Intelligent Classification Models for Rock Burst Prediction after Recognizing Significant Predictor Variables, Section 2: Designing Classifiers. *Tunn. Undergr. Space Technol.* **2019**, *84*, 522–537. [CrossRef]
36. Wang, X.; Li, S.; Xu, Z.; Xue, Y.; Hu, J.; Li, Z.; Zhang, B. An Interval Fuzzy Comprehensive Assessment Method for Rock Burst in Underground Caverns and Its Engineering Application. *Bull. Eng. Geol. Environ.* **2019**, *78*, 5161–5176. [CrossRef]
37. Pu, T. Elastic Properties of Neoproterozoic Rocks from Xuefeng Mounain Belt, South China. *Geo. J. CHN Univ.* **2024**, *30*, 72–88.
38. Fan, H.; Li, L.; Liu, H.; Hu, J.; Zhang, M.; Zhou, S.; Yang, G. Improvement to the calculating model of the pressure arch's height considering the confining pressure in the excavation of shallow tunnels. *Arab. J. Geosci.* **2021**, *14*, 1130. [CrossRef]
39. Kong, X.; Liu, Q.; Zhang, Q.; Wu, Y.; Zhao, J. A method to estimate the pressure arch formation above underground excavation in rock mass. *Tunn. Undergr. Space Technol.* **2018**, *71*, 382–390. [CrossRef]
40. Russenes, B.F. Analysis of Rock Spalling for Tunnels in Steep Valley Sides. Master's Thesis, Department of Geology, Norwegian Institute of Technology, Trondheim, Norway, 1974; 247p. (In Norwegian).

Disclaimer/Publisher's Note: The statements, opinions and data contained in all publications are solely those of the individual author(s) and contributor(s) and not of MDPI and/or the editor(s). MDPI and/or the editor(s) disclaim responsibility for any injury to people or property resulting from any ideas, methods, instructions or products referred to in the content.